

# Engineering the Hypersonic Phononic Band Gap of Hybrid Bragg Stacks

Dirk Schneider,<sup>†</sup> Faroha Liaqat,<sup>‡</sup> El Houssaine El Boudouti,<sup>§</sup> Youssef El Hassouani,<sup>||</sup> Bahram Djafari-Rouhani,<sup>⊥</sup> Wolfgang Tremel,<sup>‡</sup> Hans-Jürgen Butt,<sup>†</sup> and George Fytas<sup>\*,†,‡,#</sup>

<sup>†</sup>Max Planck Institute for Polymer Research, Ackermannweg 10, 55128 Mainz, Germany

<sup>‡</sup>Johannes Gutenberg University, Duesbergweg 10–14, 55128 Mainz, Germany

<sup>§</sup>LDOM, Département de Physique, Faculté des Sciences, Université Mohamed I, 60000 Oujda, Morocco

<sup>||</sup>Département de Physique, Faculté des Sciences et Techniques, Université Moulay Ismaïl, Boutalamine 52000, Errachidia, Morocco

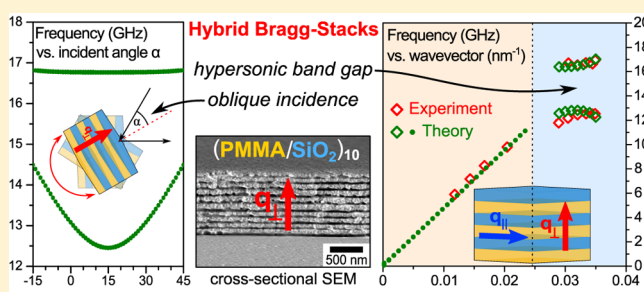
<sup>⊥</sup>Institut d'électronique, de Microélectronique et de Nanotechnologie (IEMN), UMR-CNRS 8520, UFR de Physique, Université de Lille 1, 59655 Villeneuve d'Ascq, France

<sup>#</sup>Department of Materials Science, University of Crete and FORTH, 71110 Heraklion, Greece

## S Supporting Information

**ABSTRACT:** We report on the full control of phononic band diagrams for periodic stacks of alternating layers of poly-(methyl methacrylate) and porous silica combining Brillouin light scattering spectroscopy and theoretical calculations. These structures exhibit large and robust on-axis band gaps determined by the longitudinal sound velocities, densities, and spacing ratio. A facile tuning of the gap width is realized at oblique incidence utilizing the vector nature of the elastic wave propagation. Off-axis propagation involves sagittal waves in the individual layers, allowing access to shear moduli at nanoscale. The full theoretical description discerns the most important features of the hypersonic one-dimensional crystals forward to a detailed understanding, a precondition to engineer dispersion relations in such structures.

**KEYWORDS:** Phononics, band gap, superlattices, hypersonic propagation, Brillouin spectroscopy



Controlling sound propagation has been an intensely studied field during the past centuries, ranging from architectural design<sup>1</sup> over noise reduction applications<sup>2,3</sup> to the rise of thermal management,<sup>4</sup> sound shields,<sup>5</sup> acoustic diodes,<sup>6</sup> and acoustic metamaterials.<sup>7,8</sup> Phononic crystals (PnC) happen to be a promising class of composite structures that allow for systematic manipulation of elastic (acoustic) wave propagation. The most striking feature is their ability to create (phononic) band gaps, similar to the electronic and photonic bandgaps in semiconductors and photonic crystals (PhC), respectively. Following the discoveries in the older field of PhC (periodic spatial variation of refractive index  $n$ ), PnCs (variation of density  $\rho$  and longitudinal  $c_L$  and transverse  $c_T$  sound velocities) happen to share many similarities, such as Bragg reflection and characteristic dispersion relations. However, elastic waves require many more parameters being considered for a full theoretical description, i.e., it renders predicted phononic behavior complicated. While the band diagram of semiconductors simply reflects scalar waves, and transverse waves in PhCs, sufficient description of sound propagation requires full vector waves.

The search for phononic structures started with theoretical work<sup>9,10</sup> in 1993. The first observation of band gaps followed later, using manually manufactured metallic macrostructures in the centimeter range with gaps at audible frequencies.<sup>11</sup>

In contrast to these sonic phononic crystals, the need to reach high frequencies in the hypersonic (GHz) range and beyond imposes substantial demand on design, fabrication, and characterization techniques because of the inherently much smaller length scale. The first phononic band gap in the hypersonic regime was experimentally observed in a three-dimensional assembly of close-packed polymer colloids,<sup>12</sup> soon after the foundation of experimental studies on 2D hypersonic crystals has been laid in 2005.<sup>13</sup> During the following years extensive research has been carried out on hypersonic phononics. The tuning and switching of high-frequency phononics<sup>12,14</sup> point forward to possible applications and underline the importance of controlled wave propagation. However, the full description of phonon propagation in multidimensional periodic assemblies still remains a challenging task.

The research on phononic band diagrams in 1D superlattices has started earlier than the discovery of complete (omnidirectional) phononic band gaps<sup>9,10</sup> with the study of folded phonons in a semiconductor superlattice using Raman spectroscopy at few laser wavelengths,<sup>15</sup> followed by other Raman studies.<sup>16–19</sup>

**Received:** March 12, 2012

**Revised:** April 13, 2012

**Published:** April 16, 2012

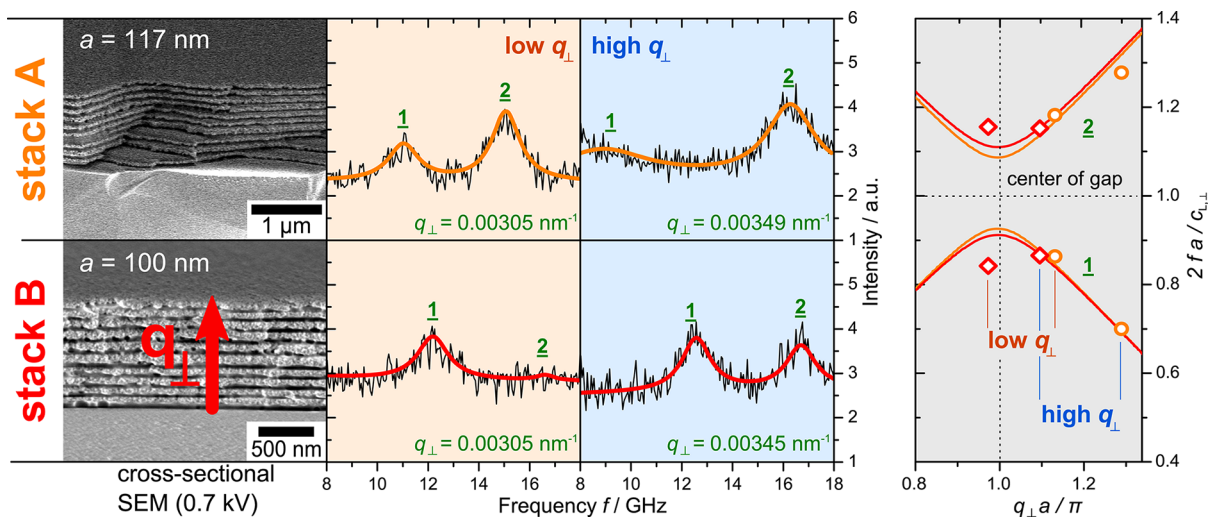


**Figure 1.** Two Bragg stacks and the phononic band gap at a glance. SEM images (left) and splitting into two phonon branches (1 and 2, middle panel). Stack A has a larger spacing  $a$  than stack B and displays only the high-frequency band (2) at high  $q_{\perp}$  directed normal to the layers (on  $z$ -axis, scheme in the left panel). The situation is inverted in stack B. The solid lines represent Lorentzian line fits used to extract the frequency  $f$  and damping  $\Gamma$  (fwhm) of modes (1) and (2) from the experimental spectra. The right panel maps the eight frequencies of the four BLS spectra (middle panel) on the normalized dispersion diagram for phonon propagation normal to the layers of the two stacks; the Bragg gap occurs at  $q_{\perp}a/\pi = 1$  and centers at  $2fa/c_{l,\perp} = 1$ , with  $c_{l,\perp}$  being the effective longitudinal sound velocity along the  $z$ -axis.

More recently, some evidence for the existence of a hypersonic band gap and zone-folded phonons and in-plane layer excitations was reported for porous silicon,<sup>20,21</sup> II–IV semiconductors,<sup>22</sup> and polymer<sup>23–25</sup> superlattices using Brillouin and pump–probe time-resolved spectroscopy. For 1D periodic structures, however, the first direct observation of a sizable normal incidence hypersonic phononic band gap was reported in periodic porous silica/poly(methyl methacrylate) (p-SiO<sub>2</sub>/PMMA) multilayer films by some of the present authors.<sup>25</sup>

The latter study has initiated new perspectives toward the engineering of phonon propagation which are addressed in the present paper. These include: (i) robustness of the dispersion to fabrication inherent imperfections; (ii) the unique estimation of both elastic moduli (longitudinal  $C_{11}$  and shear  $C_{44}$ ) and elastooptic coefficients of the individual layers; (iii) the theoretical representation of the dispersion relations for normal and oblique incidence; and (iv) the intensities of the two, lower and upper, phononic branches of the gap. On the basis of these findings, we expect new designs of nanostructures to emerge for desired direction-dependent elastic wave propagation and profound (hypersonic) phonon–(visible) photon interactions.

**Results and Discussion.** Stacks of PMMA and p-SiO<sub>2</sub> were assembled by alternating spin coating from the respective stock solutions on a cleaned glass substrate starting with the PMMA layer. Two multilayer stacks each consisting of 20 alternating PMMA and p-SiO<sub>2</sub> layers with different thicknesses  $d_{\text{PMMA}}$  and  $d_{\text{SiO}_2}$  and hence periodicity,  $a = d_{\text{PMMA}} + d_{\text{SiO}_2}$ , were fabricated. A combination of scanning electron microscopy (SEM) and confocal microscopy was used to determine the relative distribution of materials and the absolute thickness of the multilayer structure. Figure 1 (left panel) displays the SEM pictures of stack A with  $a = 117$  nm ( $d_{\text{SiO}_2} = 79 \pm 6$  and  $d_{\text{PMMA}} = 38 \pm 4$  nm) and stack B with  $a = 100$  nm ( $d_{\text{SiO}_2} = 55 \pm 5$  and  $d_{\text{PMMA}} = 45 \pm 5$  nm).

We used the nondestructive technique of spontaneous Brillouin light scattering (BLS) spectroscopy to probe hypersonic phonons propagating in these structures at submicrometer scale and thermal equilibrium. BLS utilizes the photoelastic interaction of an incident visible photon (532 nm) and a thermally excited

phonon with wavevector  $\mathbf{k}$  and frequency,  $\omega = 2\pi f$ , in the sample. The phonon energy is represented by the frequency shift ( $\omega$ ) of inelastically scattered light of a single-mode laser beam. The small shift (of the order of few GHz) is resolved by a six-pass tandem Fabry–Pérot interferometer. For a homogeneous medium, the probed phonon has  $\mathbf{k}$  equal to the scattering wavevector  $\mathbf{q} = \mathbf{k}_s - \mathbf{k}_i$  (here  $\mathbf{k}_s$  and  $\mathbf{k}_i$  are the wavevectors of the scattered light and incident laser beam). For a periodic structure with a reciprocal lattice vector  $\mathbf{G}$ , momentum conservation requires  $\mathbf{k} = \mathbf{q} + \mathbf{G}$ . The desired dispersion relation is represented by the plot  $\omega(\mathbf{k})$  along a propagation direction selected by the scattering geometry.<sup>25</sup> Along the periodicity direction (on-axis),  $q = q_{\perp}$  is perpendicular to the layers (hence,  $q_{\parallel} = 0$ ), whereas in-plane propagation is probed for  $q = q_{\parallel}$  along the layers (and hence  $q_{\perp} = 0$ ) at oblique incidence,  $q_{\perp}, q_{\parallel} \neq 0$  (off-axis).

Figure 1 displays BLS spectra for stacks A and B, both for two  $q_{\perp}$  values near the edge of the first Brillouin zone (BZ) appearing at  $\mathbf{G}/2 = \pi/a$ , i.e.,  $q_{\text{BZ}} = 0.0269$  and  $0.0314$  nm<sup>−1</sup>, respectively, for stacks A and B. The double-peak structure of the BLS spectra corresponds to the bands (1) and (2) (at low and high frequency, respectively) between which the Bragg gap occurs. The different spacing of the two films is manifested in the BLS spectral shape (Figure 1); stack A (periodicity  $a = 117$  nm) shows mainly branch (2) with branch (1) at about 9 GHz being very weak (see also Figure 2a), while stack B ( $a = 100$  nm) displays both branches at the high  $q_{\perp}$  value in the right panel of Figure 1. The BLS spectra correspond to different  $q_{\perp}a$  values, and their shape sensitively depends on the proximity to the edge of the BZ at  $q_{\perp}a = \pi$ .

Both stacks were scanned through the accessible  $q$ -range (methods) to obtain the dispersion relation  $f(q_{\perp})$  for on-axis phonon propagation (yellow circles/red diamonds on blue ground in Figure 2c). The BLS spectra were well represented by a double Lorentzian convoluted with the instrumental function (Figure 1); the solid lines in Figure 2a represent the theoretical spectra. The line intensities and the peak frequencies are shown in Figure 2b,c (blue shaded area), respectively. Figure 2c also includes the phonon frequencies for

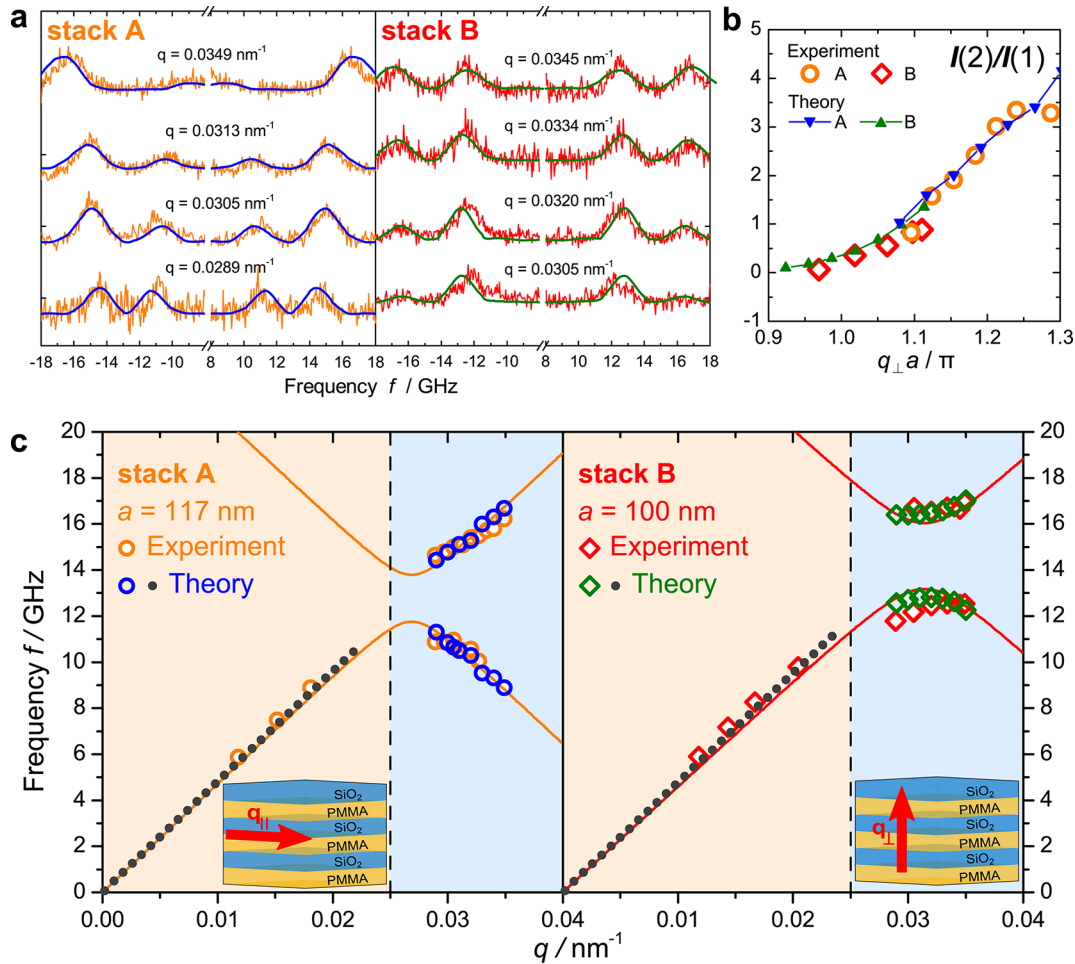


**Figure 2.** (a) Experimental BLS spectra of the stack A and B superimposed with the theoretical spectra (solid lines) at different phonon wavevectors  $q_{\perp}$  normal to the layers. (b) The ratio  $I(2)/I(1)$  of the intensities of the high- and low-frequency bands in (a). The small-size symbols indicate the values of  $I(2)/I(1)$  obtained from the theoretical spectra in (a). (c) Dispersion relation of stacks A and B (experimental data given in yellow circles/red diamonds) for in- (reddish back) and out-of-plane (light blue back) propagation separated by the vertical dashed lines. The solid lines denote the theoretical dispersion relation eq 5 for sound propagation along the periodicity axis (scheme for  $q_{\perp}$ ) in the range  $0 < q_{\perp} < 0.04$  nm<sup>-1</sup> and hollow symbols indicate the mode (1) and (2) frequencies obtained from the theoretical spectra in (a). The linear dispersion for phonon propagation parallel to the stacks (scheme for  $q_{\parallel}$ ) is denoted as a dotted line along with the experimental data along the same direction. Note that the solid lines (referring to  $q_{\perp}$ ) and the dotted lines (referring to  $q_{\parallel}$ ) do not coincide indicating different effective medium sound velocities along the two directions.

in-plane propagation (reddish area) in the two hybrid stacks. The opening of a hypersonic phononic stop band along the periodicity direction (at  $q_{\perp}a = \pi$ ) is demonstrated with the two stacks covering different regimes in the BZ; stack A falls mainly into the second BZ. In spite of the (small) differences in the elastic parameters (Table 1), the intensity ratio  $I(2)/I(1)$  of the two bands superimpose on a common curve when plotted versus  $q_{\perp}a$  in Figure 2b, thereby justifying the larger ratio observed for stack A (Figures 1 and 2a). The intensities  $I(1)$  and  $I(2)$  of the two first-folded modes depend on the relative fraction of the two layers, while the strong variation of  $I(2)/I(1)$  is predicted<sup>26</sup> at the edge of the first BZ.

A detailed understanding of the phononic properties of 1D crystals requires the full description of the experimental BLS spectrum that involves the concurrent representation of both intensities of the two modes and the dispersion relations. The computation of the full BLS spectrum is based on the calculation of the density of vibrational states (DOS) and the ratio of elasto-optic coefficients in PMMA and p-SiO<sub>2</sub>, which couple material displacements with refractive index fluctuations.

The density of states  $n(\omega, k)$  is calculated by using the Green's function technique and the theory of interface response in the frame of elasticity theory.<sup>27</sup> This formalism enabled us to calculate the displacement field at any point inside the composite material, particularly the reflected and transmitted waves. The dispersion relations of propagating and localized modes are given by the determinant of the inverse Green's function of the interface space  $g(MM)$ :

$$\det[g(MM)]^{-1} = 0 \quad (1)$$

The details of calculation of the Green's function in the space of interfaces  $M$  separating the layers as well as the calculation of local and total densities of states are given elsewhere.<sup>27</sup> The propagation of an acoustic wave in the superlattice excites periodic variations of strain which in turn induce a modulation of the dielectric tensor  $\epsilon_{\alpha}$  in the medium  $\alpha$  due to its photoelastic coupling to elastic fluctuations:

$$\delta\epsilon_{\alpha} = p_{\alpha} \frac{\partial u_{\alpha}(z)}{\partial z} \quad (2)$$



**Table 1. Values of the Physical Quantities Used in the Calculations<sup>a</sup>**

		PMMA	p-SiO <sub>2</sub>	substrate
A	$c_L$ , m s <sup>-1</sup>	2800 <sup>b</sup>	3100	5600
	$c_T$ , m s <sup>-1</sup>	1400 <sup>b</sup>	1800	
	$\rho$ , kg m <sup>-3</sup>	1190 <sup>b</sup>	1420	2200
	$d$ , nm	38	79	
	$p_{\text{PMMA}}/p_{\text{SiO}_2}$	2		
	$n$	1.49	1.46	1.53
B	$c_L$ , m s <sup>-1</sup>	2800 <sup>b</sup>	3030	5600
	$c_T$ , m s <sup>-1</sup>	1400 <sup>b</sup>	1800	
	$\rho$ , kg m <sup>-3</sup>	1190 <sup>b</sup>	1500	2200
	$d$ , nm	45	55	
	$p_{\text{PMMA}}/p_{\text{SiO}_2}$	2		
	$n$	1.49	1.46	1.53

<sup>a</sup>Sound velocities ( $c_L$ ,  $c_T$ ), density ( $\rho$ ), thickness ( $d$ ), refractive index ( $n$ ). <sup>b</sup>These parameters were fixed to the values of bulk PMMA film.<sup>25,29</sup>

Equation 2 relates the dielectric fluctuation in each medium  $\alpha$  (PMMA or SiO<sub>2</sub>) to the longitudinal displacement field along the periodicity direction  $z$  (on-axis) via the photoelastic constant  $p_\alpha = -\varepsilon_\alpha^2 P_{1133}^\alpha$ , with  $P_{1133}^\alpha$  being the photoelastic tensor in medium  $\alpha$  along  $x = 1$  and  $z = 3$  directions.

This coupling between incident light and phonons is the source of the scattered field  $E_s(\omega, q_\perp)$  from the superlattice. In general, the calculation is performed by taking into account elastic and optical modulation of the layers as well as the modulation  $\delta\varepsilon$  caused by the displacement of the interface because of the strain (i.e., the opto-mechanical effect). However, the dielectric modulation of the multilayer structure can be neglected when the layers are thin (<100 nm) as compared to the probing optical wavelength (532 nm). The same is true if the layers are characterized by almost the same refractive indices. In this particular case the system can be considered as an homogeneous medium from the optical point of view and  $E_s(\omega, q_\perp)$  becomes

$$E_s(\omega, q_\perp) \propto \sum_\alpha \int e^{iq_\perp z'} p_\alpha \frac{\partial u_\alpha(z', \omega)}{\partial z'} dz' \quad (3)$$

Hence, the scattered intensity is given by

$$I_s(\omega, q_\perp) \propto \left| \sum_\alpha \int p_\alpha e^{iq_\perp z'} \frac{\partial u_\alpha(z', \omega)}{\partial z'} dz' \right|^2 \quad (4)$$

The solid lines in Figure 2a denote the fit of  $I_s(\omega, q_\perp) \propto |E_s(\omega, q_\perp)|^2$  to the BLS spectra using the values of the parameters listed in Table 1. The computed  $I(2)/I(1)$  ratio (solid symbols in Figure 2b) and the frequencies of modes (1) and (2) (blue and green symbols on the right shaded areas in Figure 2c) in the dispersion relations of the two stacks are in good agreement with the corresponding experimental values. In fact, extrapolation (not shown in Figure 2b) of the theoretical calculations for stack B at higher  $q_\perp a/\pi$  values (between 1.1–1.3) lead to slightly lower intensity ratios than observed in stack A. The on-axis dispersion diagram in the

present 1D phononic crystals was found to be well represented (solid lines in Figure 2c) by<sup>28</sup>

$$\cos(ka) = \cos\left(\frac{\omega d_{\text{SiO}_2}}{c_{L,\text{SiO}_2}}\right) \cos\left(\frac{\omega d_{\text{PMMA}}}{c_{L,\text{PMMA}}}\right) - \frac{1}{2} \left( \frac{Z_{\text{SiO}_2}}{Z_{\text{PMMA}}} + \frac{Z_{\text{PMMA}}}{Z_{\text{SiO}_2}} \right) \sin\left(\frac{\omega d_{\text{SiO}_2}}{c_{L,\text{SiO}_2}}\right) \sin\left(\frac{\omega d_{\text{PMMA}}}{c_{L,\text{PMMA}}}\right) \quad (5)$$

with  $Z = \rho c_L$  being the longitudinal elastic impedance of the two layers. In the computation of the dispersion relations, we utilized the values of the parameters (Table 1) as obtained from the representation of the experimental spectra (Figure 2). Hence, the description of the dispersion relations in Figure 2c by eq 5 is noticeable.

The effective medium longitudinal sound velocity  $c_{L,\perp}$  amounts to 2970 ms<sup>-1</sup> in stack A and 2890 ms<sup>-1</sup> in stack B (slope of eq 5 in the low- $q$  limit). In fact, these values can be also computed from Wood's law,<sup>30</sup> which is obtained by Taylor expansion of eq 5 around  $\omega = 0$ :

$$\frac{1}{M(A/B)} = \frac{\phi}{\rho_{\text{PMMA}} c_{L,\text{PMMA}}^2} + \frac{1-\phi}{\rho_{\text{SiO}_2} c_{L,\text{SiO}_2}^2} \quad (6)$$

whereas  $M = C_{11} = \rho_{\text{eff}} c_{L,\perp}^2$  is the bulk modulus of the whole system (stack A or B) with an effective density of  $\rho_{\text{eff}} = \phi \rho_{\text{PMMA}} + (1-\phi) \rho_{\text{SiO}_2}$  and volume fraction  $\phi = d_{\text{PMMA}}/a$ .

The frequency of band (1) below the gap (reddish area in Figure 2c but for  $q_\perp$  associated with the solid lines) deviates from the corresponding frequency (experimental symbols) for in-plane propagation in both stacks. In the direction parallel to the layers, the effective medium sound velocity  $c_{L,\parallel}$  is a different average of the elastic properties in the individual layers, as it is affected by sagittal modes. In fact, the computed in-plane acoustic phonon frequency<sup>31</sup> (dots in the reddish area of Figure 2c) agrees well with the experimental frequencies along the same direction. The slopes of these dotted lines, i.e., the sound velocities for in-plane propagation  $c_{L,\parallel}(A) = 3020$  m/s and  $c_{L,\parallel}(B) = 2990$  m/s are slightly higher than the corresponding  $c_{L,\perp}$ , respectively. This small difference might suggest a low (<5%) mechanical anisotropy normal and parallel to the layers.

In order to provide a measure for the width of the band gap, we first look at two exemplary situations. If we assume that  $d_{\text{SiO}_2}/c_{L,\text{SiO}_2} = 2(d_{\text{PMMA}}/c_{L,\text{PMMA}})$ , exemplified by stack A, the frequencies of the upper/lower limit of the gap are given exactly by

$$f_{1,2} = \frac{c_{L,\text{PMMA}}}{2\pi d_{\text{PMMA}}} \cos^{-1} \left( \frac{Z_{\text{PMMA},\text{SiO}_2}}{Z_{\text{PMMA}} + Z_{\text{SiO}_2}} \right) \quad (7)$$

The obtained gap width of  $\Delta f = f_2 - f_1 \sim 2$  GHz is in good agreement with the band gap in stack A. Now, if we assume  $d_{\text{PMMA}}/c_{L,\text{PMMA}} = (d_{\text{SiO}_2}/c_{L,\text{SiO}_2})$ , approximately fulfilled in stack B, the center of the first gap conforms to  $f_0 d_{\text{PMMA}}/c_{L,\text{PMMA}} = f_0 d_{\text{SiO}_2}/c_{L,\text{SiO}_2} = 1/4$ , i.e., the system acts as a “quarter wave stack” exhibiting the widest possible band gap in 1D crystals.<sup>32</sup>

$$f_{1,2} = f_0 \pm \frac{2f_0}{\pi} \sin^{-1} \left( \frac{Z_{\text{PMMA}} - Z_{\text{SiO}_2}}{Z_{\text{PMMA}} + Z_{\text{SiO}_2}} \right) \quad (8)$$

with  $f_0$  being the frequency of the center of the gap at  $k_{\text{BZ}} = \pi/a$ . The larger gap width in stack B is  $\Delta f \sim 3$  GHz according to eq 8

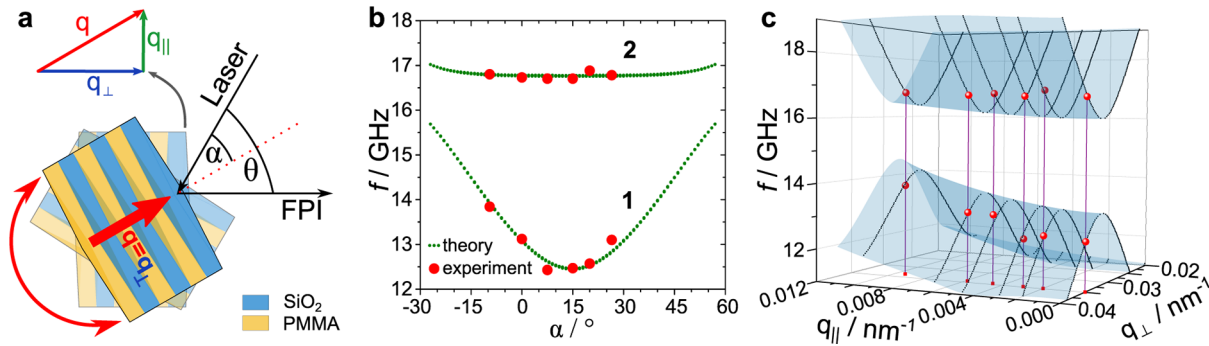


**Figure 3.** Oblique phonon propagation and impact on the dispersion relation. (a) Scheme of experimental geometry. Laser and detector remain at fixed positions, while the stack itself is turned around the normal of the scattering plane;  $\alpha$  varies at constant  $\theta$  ( $= 150^\circ$ ). (b) Frequency for the low- (1) and high- (2) frequency Bragg modes in stack B as a function of the incident angle  $\alpha$ . (c) Theoretical dispersion relation  $f(q_{\parallel}, q_{\perp})$  around the center of the longitudinal acoustic band gap is illustrated in a 3D surface. The experimental data obtained at various  $\alpha$  are depicted in red (shaded if below the surface), and the theoretical dispersions  $f(q_{\perp})$  at different  $q_{\parallel}$  are presented by dotted lines.

and in good agreement with the experimentally observed band gap. For quarter wavelengths layers at normal incidence, eq 8 is the same as the expression reported for 1D omnidirectional photonics.<sup>33</sup>

Aside of these two special cases and for relatively small contrast in elastic impedance  $\Delta Z/\bar{Z}$  (which is the case here), the width of the band gap can be approximated by a general expression:<sup>34</sup>

$$\Delta f \cong 2f_0/\pi \sin \frac{\pi d_{\text{PMMA}} c_{\text{L,SiO}_2}}{d_{\text{PMMA}} c_{\text{L,SiO}_2} + d_{\text{SiO}_2} c_{\text{L,PMMA}}} \frac{\Delta Z}{\bar{Z}} \quad (9)$$

where  $\Delta Z = |Z_{\text{PMMA}} - Z_{\text{SiO}_2}|$ ,  $\bar{Z} = (Z_{\text{PMMA}} Z_{\text{SiO}_2})^{1/2}$  and  $f_0$  is obtained from  $(1/2f_0) = (d_{\text{PMMA}}/c_{\text{L,PMMA}}) + (d_{\text{SiO}_2}/c_{\text{L,SiO}_2})$ . Note that  $f_0$  defines the middle of the gap only in the case of a “quarter wave stack”, where the gap width is maximized. The fundamental quantity of 1D phononic crystals, the width of their primary band gap, depends on many parameters, such as thickness and sound velocity of constituent materials and not just from the impedance mismatch  $\Delta Z/\bar{Z}$ , although this plays a central role (Figure 5);  $\Delta Z/\bar{Z} \sim 0.37$  for the present PMMA and p-SiO<sub>2</sub> layers.

For small elastic contrast, eqs 7–9 yield two simple equations for stop bandwidth of stacks A ( $d_{\text{PMMA}}/d_{\text{SiO}_2} \approx 0.5$ ) and B ( $d_{\text{PMMA}}/d_{\text{SiO}_2} \approx 1$ ), respectively:

$$\Delta f \cong \frac{\sqrt{3}}{6} \frac{c_{\text{L,PMMA}}}{\pi d_{\text{PMMA}}} \frac{\Delta Z}{\bar{Z}} \approx 1.8 \text{ GHz} \quad (10)$$

and

$$\Delta f \cong \frac{1}{2} \frac{c_{\text{L,PMMA}}}{\pi d_{\text{PMMA}}} \frac{\Delta Z}{\bar{Z}} \approx 3 \text{ GHz} \quad (11)$$

The observed good agreement between theory and experiment leads to important conclusions: (i) The phononic dispersion is not simply scalable with the mismatch of elastic impedance  $\Delta Z/\bar{Z}$ . In contrast to photonics, density and sound velocity of both layers enter explicitly in eq 5; (ii) the physical quantities, density, and longitudinal elastic modulus of the porous SiO<sub>2</sub> layer adopt lower values than in silica glass; these are slightly different in the two stacks; (iii) the average thicknesses of the individual layers are uniquely obtained; and (iv) effective medium elastic parameters ( $\rho, c_{\text{L},\perp}$ ) are also obtained from the frequency of mode (1) which becomes acoustic only at low  $q_{\perp}$ 's.

A versatile tuning of the phononic band structure is feasible by simply turning the film around its axis normal to the scattering plane (sagittal plane) as visualized in Figure 3a. This leads to an oblique incidence at which the scattering wavevector  $\mathbf{q}$  deviates from  $q_{\perp}$  activating mixing with sagittal modes, i.e., in-plane propagating transverse modes. Yet,  $\mathbf{q}$  is represented by a linear combination of  $q_{\perp}$  and  $q_{\parallel}$ , that is a function of the scattering angle  $\theta$  and the incident angle  $\alpha$  (eqs 12a–12c).

$$q_{\parallel} = q \cdot \sin \left[ \frac{1}{2} \left( \sin^{-1} \left( \frac{1}{n} \sin \alpha \right) - \sin^{-1} \left( \frac{1}{n} \sin(\alpha + \theta) \right) \right) \right] \quad (12a)$$

$$q_{\perp} = q \cdot \cos \left[ \frac{1}{2} \left( \sin^{-1} \left( \frac{1}{n} \sin \alpha \right) - \sin^{-1} \left( \frac{1}{n} \sin(\alpha + \theta) \right) \right) \right] \quad (12b)$$

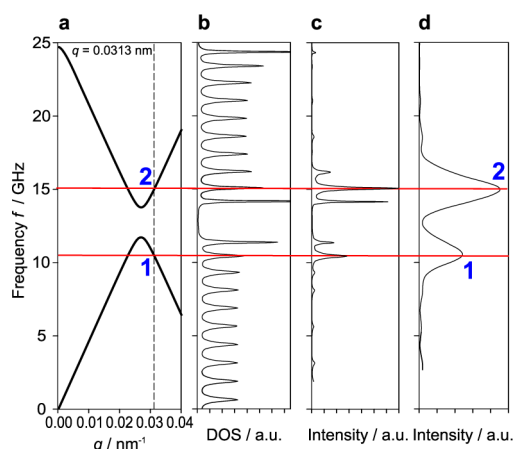
$$q = \sqrt{q_{\parallel}^2 + q_{\perp}^2} \quad (12c)$$

Figure 3b depicts the phonon frequencies of modes (1) and (2) as function of the incidence angle in stack B (at  $\theta = 150^\circ$ ). As  $\alpha$  deviates from  $(\pi - \theta)/2$  ( $= 15^\circ$ ) the low-frequency mode (1) approaches the high-frequency mode (2), which is remarkably robust to the incidence angle in agreement with the theoretical calculations (dotted lines); the latter predict the same behavior for stack A. The fact that the frequency of mode (2) is independent of  $\alpha$  does not imply that it is independent of  $q_{\perp}$  and  $q_{\parallel}$  since both modes are dispersive. The angle  $\alpha = (\pi - \theta)/2$ , at which the minimum of the frequency of branch (1) occurs, corresponds to the perpendicular propagation where only longitudinal modes are involved. Away from this  $\alpha$  value, the longitudinal modes convert to transverse modes.<sup>35</sup> Calculations confirmed that mode (2) remains mostly longitudinal with an almost constant frequency, whereas for the lower frequency Bragg mode (1) a partial mixing of polarizations occurs. This is manifested by strong lifting of degeneracy in the computed dispersion at increased  $q_{\parallel}$  (i.e., far from  $\alpha = 15^\circ$ ) leading to an increasing frequency (Figure 3b).

We note that the experimental frequencies (dots in Figure 3b) do not fall at the edge of the BZ. The locus of the two mode frequencies in the three-dimensional dispersion diagram is better seen in Figure 3c along with the theoretical dispersion relations (dotted lines) plotted as a function of both  $q_{\perp}$  and  $q_{\parallel}$ . Furthermore, the gap width narrows with increasing  $q_{\parallel}$  or obliqueness. The mixing of the longitudinal with the transverse

phonons becomes advantageous since it allows the estimation of the shear moduli of the individual layers. The computed frequencies of modes (1) and (2) using the shear velocity  $c_{T,\text{SiO}_2}$  (Table 1) as adjustable parameter capture the experiment very well (Figure 3b,c). Thus, implementation of particular sample rotation (Figure 3) is beneficial as it allows ease tuning of the gap and concurrent determination of the shear moduli which are inaccessible for normal incidence wave propagation. Oblique incidence for 1D phononics is more complicated than for 1D photonic structures,<sup>33</sup> since TE and TM modes are decoupled in the latter.

Figure 4 contrasts the theoretical prediction of the modes near the edge of the BZ of an ideal 1D periodic structure with



**Figure 4.** Dispersion curve at normal incidence (a), DOS (b), and two modeled spectra of different resolutions (c,d) at  $q = 0.0313 \text{ nm}^{-1}$  (vertical dashed line in a). The line width (fwhm) of the peaks in the DOS (b) is  $\sim 0.25 \text{ GHz}$ , and the theoretical spectrum in (c) is a triplet spectral structure for each of the two Bragg bands (1) and (2) with maximum frequencies arising at  $f$  fixed by  $q_{\perp}$  in the dispersion curve (a) (red guides). The triplet structure in (c) is smeared out to the experimental doublet (d) due to the reduced resolution ( $\Gamma = 0.53 \text{ GHz}$ ).

the experimental doublet of the BLS spectrum for stack A at a constant  $q_{\perp}$ . Figure 4a shows the theoretical dispersion relation, while Figure 4b displays the calculated DOS with 10 sharp peaks for each branch in the BZ equivalent to the number of periods in the stack. The peak separation is about  $1.2 \text{ GHz}$  in the DOS diagram, while their inherent broadening ( $\Gamma^* \sim 0.25 \text{ GHz}$ , even smaller near the gap) is due to interaction of the superlattice discrete modes with the substrate continuum as these modes are propagating within the substrate. The modeled spectrum, displayed in Figure 4c for  $q_{\perp} = 0.0313 \text{ nm}^{-1}$  (vertical dashed line in Figure 4a), exhibits a triplet spectral structure, and the maximum occurs at the fixed  $q_{\perp}$ . From the different modes of the DOS (Figure 4b), only the modes falling around the frequencies (red lines in Figure 4) at the selected  $q_{\perp}$  contribute to the theoretical spectrum (Figure 4c). The latter had to be convoluted with the instrumental function (Gaussian with  $\Gamma \sim 2\Gamma^* \sim 0.53 \text{ GHz}$ ) to match the doublet shape of the experimental spectrum in Figure 4d associated with the dispersion diagram of the infinite structure (eq 5 and Figure 2c).

In order to elucidate the impact of unavoidable interfacial defects of layers (SEM pictures in Figure 1), we note that state-of-the-art hybrid (inorganic/polymer) spin coating cannot yet compete with semiconductor production techniques, e.g., molecular beam epitaxy, in terms of roughness and structural coherence. However, the

roughness is much smaller than the layer thicknesses, and phonon wavelengths in the submicrometer range should render the scattering losses weak.

We therefore consider theoretically the effect of structural disorder exemplified by incoherent spacing. Figure 5a shows the experimental BLS spectrum of stack A at  $q_{\perp} = 0.0313 \text{ nm}^{-1}$  along with the computed spectrum indicated by the solid line as already shown in Figure 4d. The sensitivity of this representative spectrum in the vicinity of the BZ to the variation of the thickness of the two constituent layers at fixed lattice constant  $a$  ( $= 117 \text{ nm}$ ) is illustrated in Figure 5b for three thickness combinations (39:78, 30:87, and 50:67) and the average spectrum over 10 000 realizations with different  $d_{\text{PMMA}}/d_{\text{SiO}_2}$  ratios, i.e., randomized volume fraction variations as suggested by the SEM images. We have also examined the effect of the independent variation of each type of layer spacing simulating thousands of structures, varying randomly the thickness of PMMA (34–44 nm) and  $\text{SiO}_2$  (73–83 nm) layers, i.e., with free lattice constant. We obtained the same results as for the mean spectrum (i.e., blue curve in Figure 5b for  $d_{\text{PMMA}} = 39 \text{ nm}$  and  $d_{\text{SiO}_2} = 78 \text{ nm}$ ).

It is remarkable that the spectral doublet is robust and that only the lower frequency band (1) undergoes a blue shift leading to a gap narrowing with decreasing  $d_{\text{PMMA}}/d_{\text{SiO}_2}$ , whereas the large sampling (dashed line in Figure 5) coincides

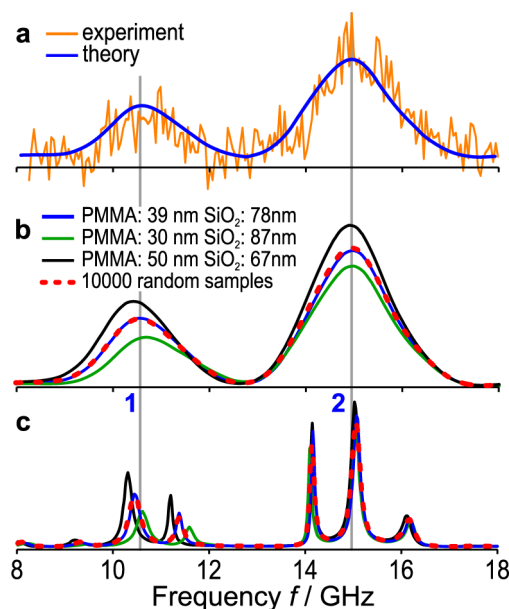


**Figure 5.** Structure incoherence. (a) The experimental BLS of stack A at  $q = 0.0313 \text{ nm}^{-1}$  along with the (low resolution) theoretical spectrum (solid line) of Figure 4d with  $d_{\text{PMMA}} = 38 \text{ nm}$  and  $d_{\text{SiO}_2} = 79 \text{ nm}$ . (b) Theoretical spectra at three different  $d_{\text{PMMA}}/d_{\text{SiO}_2}$  ratios (solid lines) but fixed spacing  $a = 117 \text{ nm}$ . The dashed curve represents a mean over 10 000 stacks of randomly chosen PMMA/p-SiO<sub>2</sub> fraction between the two extrema ( $30 \leq d_{\text{PMMA}} \leq 50 \text{ nm}$ ). (c) High-resolution theoretical spectra without instrumental broadening corresponding to the four cases in (b) (cf. Figure 4c).

with the spectrum for  $d_{\text{PMMA}}/d_{\text{SiO}_2} = 0.5$  ( $\sim 39/78$ ). The gap widening at increased volume fractions of PMMA as well as the asymmetric shift of the low- and high-frequency peak are captured by eqs 7–9. This predicted trend is clearly seen in the nonconvoluted spectra of Figure 5c which indicates that the smearing of the triplet structure for both bands (1) and



(2) (Figure 5b) cannot be singly attributed to the particular kind of disorder (structure incoherence). It is worth mentioning that over about 16% variation of the volume fraction of the p-SiO<sub>2</sub> layers (or about 20% for the PMMA layers), the spectral widths for both branches in Figure 5b are robust; this spacing variation conforms to the paracrystalline lattice distortion parameter (13% for both stacks) estimated from the SEM images.<sup>36</sup> We therefore conclude that the smearing due to disorder is less than the experimental resolution, hence its effect can only be evaluated if the instrumental resolution could be significantly improved.

**Conclusions.** One-dimensional periodic hybrid phononic structures act as a model system for a fundamental understanding of elastic wave propagation in nanostructured matter. A phononic “Bragg” gap opens for wave propagation along the periodicity direction, i.e., normal incidence. The width, the frequency at the center of the gap, and the intensities of the lower and upper frequency Bragg modes are all well described theoretically. The concurrent representation of the phonon dispersion and the amplitudes of the modes leads to the estimation of the longitudinal sound velocity along the layer normal and density of the individual layers. Inherent fabrication-related film imperfections, such as inhomogeneous layer thicknesses, lead to a smearing of the position of the lower Bragg mode. However, the width of the gap remains constant in the course of the examined thickness variations as indicated by the simulations.

Tuning of the gap position and width is readily obtained by rotation of the stack around the axis normal to the sagittal plane of the film. At such oblique incidence due to the vector nature of the elastic wave propagation, mixing with in-plane sagittal modes allows the estimation of the shear moduli of the individual layers at nanoscale. Access to both moduli opens a new way to investigate material behavior under confinement and addresses direction-dependent mechanical properties.

The complete description of 1D hybrid phononics, i.e., experimental dispersion relations and the DOS of 1D hybrid stacks, creates the fundamental knowledge necessary to engineer the band structure of high-frequency phononics. Introduction of defect layers and design of dual gap structures for both photons in the visible and hypersonic phonons look now more feasible.<sup>37</sup> Over the electron and photon propagation, the phonon band structure is a complex reflection of both structure and elastic properties of the constituent media, rendering the phonon–matter interaction nontrivial.

This work is the first demonstration of the utility of soft matter fabrication techniques in hypersonic phononics. As compared with classical semiconductor fabrication techniques leading to high-quality periodic structures at shorter length scales, the present hybrid hypersonic structures possess distinct advantages, such as facile tuning of the elastic impedance contrast, realization of large phonon band gaps, and good perspectives for strong interactions of hypersonic phonons with visible photons. In addition, the reach of polymer and colloid science enables a wealth of soft periodic structures with ease tunability. Yet, their quality can be significantly improved using, e.g., interference lithography fabrication techniques.<sup>13,38</sup>

## ■ ASSOCIATED CONTENT

### ■ Supporting Information

Detailed description of the preparation and characterization methods. This material is available free of charge via the Internet at <http://pubs.acs.org>.

## ■ AUTHOR INFORMATION

### Corresponding Author

\*E-mail: [fytas@mpip-mainz.mpg.de](mailto:fytas@mpip-mainz.mpg.de).

### Notes

The authors declare no competing financial interest.

## ■ ACKNOWLEDGMENTS

DFG (grant no. BU 1556 and IRTG 1404) and GSRT of Greece (ARISTEIA program) are acknowledged for partial financial support. Three of the authors (EHEB, YEH and BDR) would like to thank the European Commission (EC) 7th Framework Programme (FP7), for support under the (IP) project reference No. 216176 (NANOPACK, [www.nanopack.org](http://www.nanopack.org)).

## ■ REFERENCES

- (1) Comerio, M. C. *Science* **2006**, *312*, 204–206.
- (2) Rao, M. D. *J. Sound Vib.* **2003**, *262*, 457–474.
- (3) Gonzalez, A.; Ferrer, M.; de Diego, M.; Piñero, G.; Garcia-Bonito, J. J. *J. Sound Vib.* **2003**, *265*, 663–679.
- (4) Pernot, G.; Stoffel, M.; Savic, I.; Pezzoli, F.; Chen, P.; Savelli, G.; Jacquot, A.; Schumann, J.; Denker, U.; Mönch, I.; Deneke, C.; Schmidt, O. G.; Rampoux, J. M.; Wang, S.; Plissonnier, M.; et al. *Nat. Mater.* **2010**, *9*, 491–495.
- (5) Gorishnyy, T.; Maldovan, M.; Ullal, C. K.; Thomas, E. L. *Phys. World* **2005**, *Dec*, 24–29.
- (6) Liang, B.; Guo, X. S.; Tu, J.; Zhang, D.; Cheng, J. C. *Nat. Mater.* **2010**, *9*, 989–992.
- (7) Fok, L.; Ambati, M.; Zhang, X. *MRS Bull.* **2008**, *33*, 931–934.
- (8) Page, J. *Nat. Mater.* **2011**, *10*, 565–566.
- (9) Kushwaha, M. S.; Halevi, P.; Dobrzynski, L.; Djafari-Rouhani, B. *Phys. Rev. Lett.* **1993**, *71*, 2022–2025.
- (10) Sigalas, M.; Economou, E. N. *Solid State Commun.* **1993**, *86*, 141–143.
- (11) Martinez-Salazar, R.; Sancho, J.; Sanchez, J. V.; Gomez, V.; Llinares, J.; Meseguer, F. *Nature* **1995**, *378*, 241–241.
- (12) Cheng, W.; Wang, J.; Jonas, U.; Fytas, G.; Stefanou, N. *Nat. Mater.* **2006**, *5*, 830–836.
- (13) Gorishnyy, T.; Ullal, C. K.; Maldovan, M.; Fytas, G.; Thomas, E. L. *Phys. Rev. Lett.* **2005**, *94*, 115501.
- (14) Jang, J.-H.; Koh, C. Y.; Bertoldi, K.; Boyce, M. C.; Thomas, E. L. *Nano Lett.* **2009**, *9*, 2113–2119 PMID: 19391612.
- (15) Colvard, C.; Merlin, R.; Klein, M. V.; Gossard, A. C. *Phys. Rev. Lett.* **1980**, *45*, 298–301.
- (16) Schwartz, G. P.; Gualtieri, G. J.; Sunder, W. A. *Appl. Phys. Lett.* **1991**, *58*, 971–973.
- (17) Zhang, P. X.; Lockwood, D. J.; Labbé, H. J.; Baribeau, J.-M. *Phys. Rev. B* **1992**, *46*, 9881–9884.
- (18) Lanzillotti Kimura, N. D.; Fainstein, A.; Jusserand, B. *Phys. Rev. B* **2005**, *71*, 041305.
- (19) Lanzillotti-Kimura, N. D.; Fainstein, A.; Huynh, A.; Perrin, B.; Jusserand, B.; Miard, A.; Lematre, A. *Phys. Rev. Lett.* **2007**, *99*, 217405.
- (20) Parsons, L. C.; Andrews, G. T. *Appl. Phys. Lett.* **2009**, *95*, 241909.
- (21) Aliev, G. N.; Goller, B.; Kovalev, D.; Snow, P. A. *Appl. Phys. Lett.* **2010**, *96*, 124101.
- (22) Berstermann, T.; Brüggemann, C.; Bombeck, M.; Akimov, A. V.; Yakovlev, D. R.; Kruse, C.; Hommel, D.; Bayer, M. *Phys. Rev. B* **2010**, *81*, 085316.
- (23) Walker, P. M.; Sharp, J. S.; Akimov, A. V.; Kent, A. J. *Appl. Phys. Lett.* **2010**, *97*, 073106.
- (24) Saini, G.; Pezeril, T.; Torchinsky, D.; Yoon, J.; Kooi, S.; Thomas, E.; Nelson, K. J. *Mater. Res.* **2007**, *22*, 719–723.
- (25) Gomopoulos, N.; Maschke, D.; Koh, C. Y.; Thomas, E. L.; Tremel, W.; Butt, H. J.; Fytas, G. *Nano Lett.* **2010**, *10*, 980–984.
- (26) He, J.; Djafari-Rouhani, B.; Sapriel, J. *Phys. Rev. B* **1988**, *37*, 4086–4098.

- (27) El Boudouti, E. H.; Djafari-Rouhani, B.; Akjouj, A.; Dobrzynski, L. *Surf. Sci. Rep.* **2009**, *64*, 471–594.
- (28) Rytov, S. M. *Sov. Phys. Acoust.* **1956**, *2*, 68.
- (29) Cheng, W.; Sainidou, R.; Burgardt, P.; Stefanou, N.; Kiyanova, A.; Efremov, M.; Fytas, G.; Nealey, P. F. *Macromolecules* **2007**, *40*, 7283–7290.
- (30) Wood, A. B. *A Textbook of Sound*; G. Bell & Sons Ltd.: New York, 1930.
- (31) Djafari-Rouhani, B.; Dobrzynski, L.; Duparc, O. H.; Camley, R. E.; Maradudin, A. A. *Phys. Rev. B* **1983**, *28*, 1711–1720.
- (32) Joannopoulos, J. D.; Johnson, S. G.; Winn, J. N.; Meade, R. D. *Photonic Crystals - Molding the Flow of Light*; Princeton University Press: Princeton, NJ, 2008; Vol. 2.
- (33) Fink, Y.; Winn, J. N.; Fan, S.; Chen, C.; Michel, J.; Joannopoulos, J. D.; Thomas, E. L. *Science* **1998**, *282*, 1679–1682.
- (34) Jusserand, B.; Paquet, D.; Mollot, F.; Alexander, F.; Le Roux, G. *Phys. Rev. B* **1987**, *35*, 2808–2817.
- (35) Kato, H.; Maris, H. J.; Tamura, S.-i. *Phys. Rev. B* **1996**, *53*, 7884–7889.
- (36) Hosemann, R.; Hindeleh, A. M. *J. Macromol. Sci., Part B: Phys.* **1995**, *34*, 327–356.
- (37) Psarobas, I. E.; Papanikolaou, N.; Stefanou, N.; Djafari-Rouhani, B.; Bonello, B.; Laude, V. *Phys. Rev. B* **2010**, *82*, 174303.
- (38) Moon, J. H.; Yang, S. *Chem. Rev.* **2010**, *110*, 547–574.

■ NOTE ADDED AFTER ASAP PUBLICATION

This paper was published ASAP on April 22, 2012. Multiple corrections have been made throughout the paper. The revised version was posted on May 1, 2012.